Journal of Power Sources 640 (2025) 236810

Contents lists available at ScienceDirect

Journal of Power Sources

journal homepage: www.elsevier.com/locate/jpowsour

Low-temperature dendrite-free Zn metal battery catalyzed by TiN-enhanced diffusion layer

Jing Zhang [a,*], Chenxiao Han [a], Lu Pan [a], Mannan Yang [a], Caiyin You [a,**], Yongzheng Zhang [e], Lujie Jia [b], Huihua Li [f], Ke Xu [g], Jian Su [a], Hongzhen Lin [b,***], Jian Wang [c,d,****]

[a] School of Materials Science and Engineering & Faculty of Printing, Packaging Engineering and Digital Media Technology, Xi'an University of Technology, Xi'an, 710048, China
[b] i-Lab & CAS Key Laboratory of Nanophotonic Materials and Devices, Suzhou Institute of Nano-tech and Nano-bionics, Chinese Academy of Sciences, Suzhou, 215123, China
[c] Helmholtz Institute Ulm (HIU), Ulm, D89081, Germany
[d] Karlsruhe Institute of Technology, Karlsruhe, D76021, Germany
[e] State Key Laboratory of Chemical Engineering, East China University of Science and Technology, Shanghai, 200237, China
[f] School of Electrical and Electronic Engineering, Harbin University of Science and Technology, Harbin, 150080, China
[g] Xi'an Shaanxi Coal Keenjoin New Energy Technology Co., Ltd, Xi'an, 713700, China

HIGHLIGHTS

- An "adsorption-sieving-catalysis" strategy has been achieved by TiN on porous RGO.
- The abundant TiN sites catalytically enhance Zn^{2+} desolvation for fast diffusion.
- Optimized Zn electrode displays long lifespan under 0 °C.

ARTICLE INFO

Keywords:
Low-temperature environment
Catalytic layer
Desolvation effect
Zn metal battery

ABSTRACT

Aqueous zinc metal batteries (AZMBs) are promising for large-scale energy storage due to their intrinsic safety and cost effectiveness. However, the cycling stability of metallic Zn anode under low temperature surroundings is severely hindered by harmful hydrogen evolution reaction (HER) and uncontrollable dendrite growth, which is ascribed to sluggish desolvation kinetics of hydrated $[Zn(H_2O)_x]^{2+}$ and blocked Zn^{2+} diffusion kinetics. Herein, the strategy of "adsorption-sieving-catalysis" is initially proposed and the titanium nitride anchored on self-assembly porous reduced graphene oxide (TiN@RGO) as functional modulator is constructed on the surface of Zn anode. The abundant electrocatalytic sites on sieving pores significantly enhance interfacial desolvation, thereby accelerating Zn^{2+} diffusion kinetics for dendrite-free plating. Consequently, TiN@RGO modified Zn delivers a long-term stripping/plating lifespan above 2600 h at 0.5 mA cm^{-2} and maintains reversible stability of 500 h at 2 mA cm^{-2} even under low temperature of 0 °C. Decreasing to as low as −8 °C, stable overpotential around 130 mV without any short-circuit is achieved. The coupled full cell with MnO_2 presents a high capacity retention of 72 % after 1000 cycles at 1.0 A g^{-1} at low temperature of 0 °C, providing new insights for the rational design of efficient LT-AZMBs.

1. Introduction

Aqueous zinc metal batteries (AZMBs) have emerged as a competitive candidate to conventional lithium-ion batteries because of their non-toxic electrolytes, improved safety with sustainable nature, and costeffectiveness [1–4]. Metallic Zn is optional in AZMBs owing to

* Corresponding author. Xi'an University of Technology, Xi'an 710048, China
** Corresponding author. Xi'an University of Technology, Xi'an 710048, China
*** Corresponding author. Suzhou Institute of Nano-tech and Nano-bionics, Chinese Academy of Sciences, Suzhou, 215123, China
**** Corresponding author. Karlsruhe Institute of Technology, Karlsruhe, D76021, Germany.
E-mail addresses: zhangjing2020@xaut.edu.cn (J. Zhang), caiyinyou@xaut.edu.cn (C. You), hzlin2010@sinano.ac.cn (H. Lin), jian.wang@kit.edu (J. Wang).

https://doi.org/10.1016/j.jpowsour.2025.236810
Received 30 January 2025; Received in revised form 3 March 2025; Accepted 13 March 2025
Available online 19 March 2025

its ultrahigh theoretical capacity (820 mA h g^{-1} and 5855 mA h cm^{-3}) and suitable redox potential (−0.76 V vs standard hydrogen electrode) [5–9]. However, the further advancement in energy-storage systems of AZMBs has greatly been hindered by parasitic side reactions of hydrogen evolution reaction (HER), anode corrosion and dendrite growth under high current density [10–13]. As the operating temperature drops to below 0 °C, the aqueous electrolyte with water solvents inevitably encounters increased viscosity with cross-linked hydrogen bond or even solidification of solvents causes viscous solvation shell with higher force, leading to sluggish desolvation and transport barriers at the electrode interface [14–19]. Owning to the sluggish evolution kinetics of large and robust $[Zn(H_2O)_x]^{2+}$ shell, the formation of dendrites becomes increasingly formidable to persistently damage battery performances, such as degraded capacity and declined Coulombic efficiency or even battery failure [20–23].

To mitigate these challenges, many efforts have been made to modulate the key steps in deal with the dissociation of $[Zn(H_2O)_x]^{2+}$ clusters to release free Zn^{2+}, including electrolyte optimization engineering, interfacial protection layers and porous sieving layers [24–36]. The typical electrolyte engineering evolving from high concentration salt electrolytes (water-in-salt) to organic additive electrolytes and hydrogel electrolytes are commonly help the dissociation of $[Zn(H_2O)_x]^{2+}$ at the expense of abandoning partial conductivity [28,37,38]. At the same time, numerous protective layers have emerged to block the direct contact of Zn metal with active water to attenuate worrisome HER and corrosion reactions [24,39–42]. To offer better desolvation effect, porous sieving morphology has been developed encompassing a spectrum of metal-organic frameworks (MOFs) and other porous materials [43–47]. By virtue of the physical sieving effect, large outer solvent clusters are screened out, whilst a small number of active water molecules fitting the pore size can pass through the pores to arrive at the Zn metal surface. Owing to the increased strength of Zn^{2+}-H_2O bond under low temperature, retarding interfacial Zn^{2+} desolvation and diffusion kinetics would impede Zn^{2+} plating/stripping processes and exacerbate undesired side reactions and dendritic growth [20,43].

Alternatively, despite porous structure allowed physical sieving of partial solvent, electrochemically catalyzing the $[Zn(H_2O)_x]^{2+}$ clusters would be more beneficial choice to chemically regulate the inner Helmholtz plane (IHP) layer to decrease desolvation barriers through fast electron/ion transfer [48–51]. Motivated by the electrochemical sieving strategy, proper structures of the catalytic materials should enable strong modulation capability to interfacial desolvation. In this regard, the Zn^{2+} transfer across the electrolyte/electrode interface would be more smoothly. As known, nano-catalysts are potentially designed to provide sufficient active sites for separating water molecules upon an energy-efficient method, which would enhance the dissociation of $[Zn(H_2O)_x]^{2+}$ into free Zn^{2+} to facilitate the diffusion kinetics [15,52]. Titanium nitride (TiN), born with desirable properties of high electron/ion conductivity and excellent chemical stability [53], has broad application prospects in the field of anode protection [54,55]. Due to the high electron/ion conductivity enabled catalytic property [56], it is still lack the attempt of “adsorption-sieving-catalysis” effect on

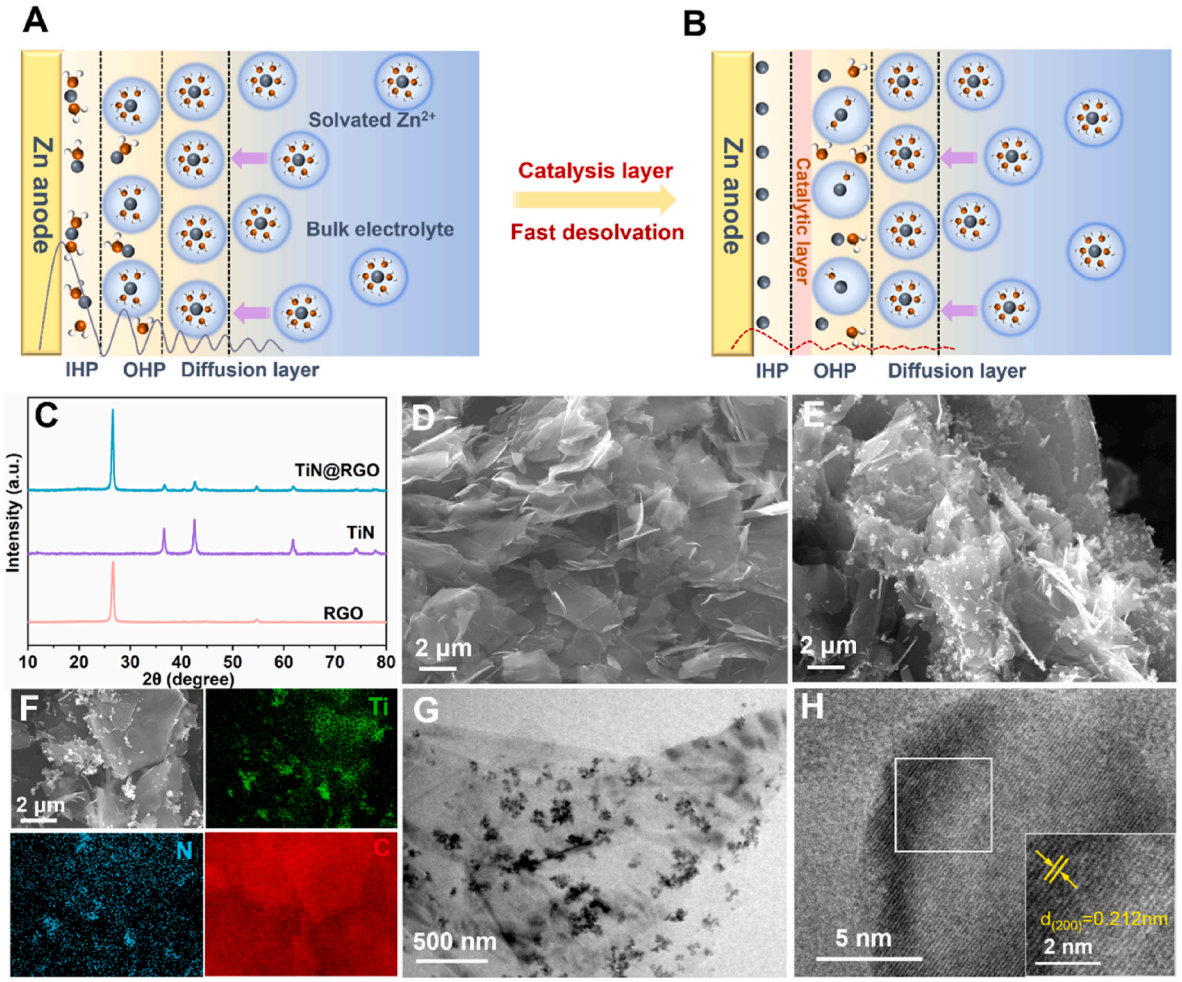

Fig. 1. (A–B) Graphical evolution of the inner Helmholtz plane in double electric layer on the Zn anode induced by TiN@RGO catalyzed layer. (C) XRD patterns of TiN, RGO and TiN@RGO nanocomposites; SEM images of (D) RGO and (E) TiN@RGO nanocomposites; (F) EDS elemental mapping on TiN@RGO nanocomposites; (G) TEM image and (H) HRTEM image of the TiN@RGO nanocomposites.

dissociating the $[Zn(H_2O)_x]^{2+}$ groups against formation of uneven Zn^{2+} flux in low-temperature surroundings.

Herein, to achieve the "adsorption-sieving-catalysis", the nanosized titanium nitride anchored on self-assembly porous reduced graphene oxide (TiN@RGO) is designed to realize fast kinetics of Zn^{2+} desolvation and diffusion against dendrite growth, which is rarely reported before. With the electrocatalysis by TiN on RGO, the TiN@RGO catalytic layer coated on Zn metal provides a large number of electrocatalytic sites and sieving pores for synergistically accelerating the desolvation of $[Zn(H_2O)_x]^{2+}$ groups to release free Zn^{2+} through "adsorption-sieving-catalysis", eliminating the uneven Zn^{2+} flux on the zinc anode to guide the following uniform Zn plating nearby the IHP layer of electric double layer (EDL), as disclosed in Fig. 1A and B. As verified by the combination investigation of optical images, wettability observation and electrochemical tests, the assembled TiN@RGO catalyst endowed with fast desolvation are beneficial to weaken the Zn^{2+}–H_2O interaction against HER occurrence, electrode erosion and dendrite growth simultaneously. Thanks to enhanced capability, the TiN@RGO modulator catalyzed Zn electrode (TiN@RGO-Zn) harvests long-term stripping/plating lifespan (2600 h) with low overpotential of 50 mV at 0.5 mA cm^{-2}. Even reducing the temperature to 0 °C, the TiN@RGO-Zn electrode still maintains reversible stability of 500 h at high current density of 2 mA cm^{-2} in deposition depth of 2 mA h cm^{-2}. Further decreasing to low temperature of −8 °C, stable overpotential around 130 mV without any short-circuit is achieved. Matching with MnO_2, the as-prepared TiN@RGO-Zn||MnO_2 full cell discloses a high capacity retention of 72 % after 1000 cycles at 1.0 A g^{-1} at low temperature of 0 °C, providing a new idea for zinc anode modification with catalytic modulation layer in achieving practical LT-AZMBs.

2. Experimental sections

2.1. Synthesis of TiN@RGO nanocomposite

TiN@RGO nanocomposite was prepared by ultrasonic peeling and following self-assembly process to anchor TiN nanoparticles on the surface of porous reduced graphene oxide (RGO). Firstly, graphene oxide powder of 234 mg (Aladdin) with 50 mg polyvinylpyrrolidone (PVP) were added to 180 mL deionized water deoxygenated before starting. The mixture was then completely dispersed in a cell wall breaking ultrasonic dispersion for 2 h. Thereafter, 59 mg of nanoscale TiN powder (Aladdin) was added to the solution and continue to ultrasonically dispersed until yielding a homogeneous blend. After stirring for 2 h, the obtained mixture was transferred into Teflon liner of stainless-steel autoclave. The sealed liner was placed in a pre-heated oven at 180 °C for 12 h. The resultant product of TiN@RGO nanocomposite was collected by filtration and later freeze-drying for 24 h. The RGO was synthesized by the same method without adding TiN nanoparticles.

2.2. Preparation of TiN@RGO-Zn anode and manganese dioxide cathode material

The as-prepared TiN@RGO powder was mixed with Super P (CANRD, China), and PVDF (HSV900, France) in NMP solution (Aladdin) in a ratio of 7:2:1 to form a homogeneous slurry. The obtained slurry was coated on a commercial zinc foil using a film blade. Then, the coated zinc foil was vacuum dried at 40 °C for 24 h to form TiN@RGO-Zn electrode, which was punched into a circular working electrode in a diameter of 16 mm for battery assembly. For preparation of MnO_2 cathode, $MnSO_4{\cdot}H_2O$ (Aladdin) of 1.014 g and $KMnO_4$ (Aladdin) of 5.688 g were put into 25 mL and 100 mL deionized water and stirred at room temperature to form homogenous solution, respectively. The $MnSO_4$ solution was added dropwise into the $KMnO_4$ solution slowly under continuously magnetic stirring. The obtained mixture was then transferred to a Teflon-lined autoclave and heated at 180 °C for 12 h. The formed precipitation was vacuum filtrated and washed with deionized water repeatedly to remove soluble impurities. The resultant solid product was dried at 110 °C for 24 h and annealed under air at 450 °C for 2 h with a heating rate of 2 °C min^{-1}. Subsequently, the as-synthesized MnO_2 powder, was mixed with Super P, and PVDF in NMP solution at a ratio of 7:2:1 to form a uniform slurry and then coated uniformly onto graphite sheet. The coated cathode was placed in a vacuum oven at 120 °C drying for 24 h, which was punched into discs of 12 mm in diameter.

2.3. Assembly of coin cells

The electrochemical performances of the cells were all evaluated on CR2025-type coin cells assembled in air atmosphere. The Zn||Zn symmetrical cell was assembled using zinc foil (TiN@RGO-Zn, RGO-Zn or bare Zn) as cathode and anode separated by commercial glass fiber (Whatman) with electrolyte containing 2 mol L^{-1} (M) $ZnSO_4$ (Aladdin). In the Zn||Cu cell, the anode was replaced by TiN@RGO modified Cu foil using the same electrolyte as the Zn||Zn symmetrical cell. The TiN@RGO-Zn||MnO_2 full battery was assembled with modified zinc foil as anode and MnO_2 discs as cathode, separated by commercial glass fiber, adding 2 M $ZnSO_4$+0.1 M $MnSO_4$ mixed solution as the electrolyte.

2.4. Materials and devices characterizations

The X-ray diffraction (XRD) patterns for collecting the crystalline structure of the samples were performed on a Smart Lab X-ray diffractometer using Cu Kα radiation in a 2θ range from 10° to 80°. The morphology of the synthesized materials and electrodes were examined using scanning electron microscopy (SEM, Zeiss Sigma HD, MERLIN, Germany) and transmission electron microscopy (TEM, JEM-ARM200CF NEOARM), respectively. Confocal microscopic images were detected on a Laser Scanning Confocal Microscope (LEXT OLS4000).

Galvanostatic charge-discharge performance of Zn||Zn symmetric cells, Zn||Cu cells and Zn||MnO_2 full cells under various current rates were all conducted on a multichannel battery test system (BTS-5 V 20 mA, Neware, China). The Tafel plots, cyclic voltammetry (CV) and electrochemical impedance spectroscopy (EIS) curves were obtained on a comprehensive electrochemical workstation (CHI660E, Shanghai). Tafel curves were performed in a three-electrode system at room temperature using a Zn plate (1 cm^{-2}) as working electrode, Pt plate as auxiliary anode and calomel electrodes (Saturated KCl) as reference electrode, respectively, at a scan rate of 1 mV s^{-1} in a 2 M $ZnSO_4$ solution. The EIS plots were performed within the frequency range from 10^{-2} to 10^5 Hz and the CV curves at constant or shifting scanning speeds were collected within a voltage range from 0.8 to 1.9 V.

3. Results and discussion

3.1. Morphology and structural characterizations on TiN@RGO nanocomposite

The TiN@RGO nanocomposite was synthesized via hydrothermal self-assembly, generating porous ion screening channel structure with abundant ion transfer promoters. As shown in the (X-Ray Diffraction) XRD pattern (Fig. 1A), the sharp peaks centered at 36.6°, 42.5° and 61.8° are definitely assigned to the planes of (111), (200) and (220) of TiN (JCPDS 87–0632) phase, whilst the apparent peaks centered at 26.6° and 54.8° can be attributed to the RGO within the TiN@RGO, indicating no phase transformation and oxidation during the synthesis. In the SEM images in Fig. 1B and C, the as-synthesized TiN@RGO nanocomposite displays the same porous morphology as the RGO, whilst the TiN nanoparticles are uniformly dispersed on the RGO substrate (Figs. 1C and S1). The EDS elemental mapping verifies the even dispersion of TiN nanoparticles in the RGO without obvious

agglomerations (Fig. 1D), due to the similar distribution of elemental Ti and N on C. The TEM images (Figs. 1E and S2) of the TiN@RGO nanocomposite further reveals the tightly anchored TiN nanoparticles without damage the self-assemble porous structure of the RGO, in which these TiN nanoparticles show a domain size of around 20 nm (Fig. S3). In the high-resolution TEM (HRTEM) image of Fig. 1F, the lattice spacing of 0.212 nm is well corresponded to the (200) crystal plane of TiN, suggesting good consistency with the XRD analysis.

3.2. Functions of TiN@RGO layer on inhibiting by product reactions

It is well known that the improved interfacial wettability is beneficial to reduce interfacial impedance formed in the contaction of active water molecules with Zn metal, stimulating the Zn^{2+} diffusion kinetics. In this way, the proportion of active water molecules within the solvation shell are pushed out, which significantly facilitate the desolvation of hydrated Zn^{2+} and undoubtedly minimize the diffusion steric hindrance of Zn^{2+}as well as mitigate the occurrence of HER. Fig. 2A and B and S4 illustrate the contact angles of the electrolyte on various electrodes, revealing that bare Zn (88°) exhibits inferior hydrophilicity in comparison to TiN@RGO (48°) and RGO (80°). Such enhanced wettability underscores the zincophilic characteristics of the TiN catalytic sites anchored on RGO (Fig. 2A). Following a natural immersion period of three weeks (Fig. 2C), the Zn electrode after removal of the TiN@RGO modification layer retains a notably smooth surface devoid of apparent corrosion (Fig. 2D and E). On the contrary, the bare Zn electrode displays a notably rougher surface indicative of severe corrosion morphology (Fig. 2D and F), characterizing by the occurrence of potential side reactions. A significant reduction in corrosion current using the TiN@RGO modification layer from 4.07×10^{-4} to 3.09×10^{-5} mA cm^{-2} is revealed in the Tafel curves of Figs. 2G and S5, which further confirms the improved corrosion resistance of the TiN@RGO-Zn electrode. According to Arrhenius equation ($Logi = -\frac{E_a}{RT} + A$), the notably reduced desolvation activation energy *Ea* (7.5 kJ vs 8.3 vs 10.8 kJ mol^{-1}) for the TiN@RGO-Zn electrode calculated from temperature dependent exchange current density (Figs. 2H and S6) underscores a significant reduce in the barrier for Zn^{2+} desolvation and an enhancement in Zn^{2+} diffusion kinetics facilitated by TiN@RGO catalytic layer. Moreover, the roughly estimated thickness of the coin cell with TiN@RGO modification layer increases the least (0.4 mm with TiN@RGO vs. 1.3 mm of bare Zn) without any electrolyte leakage after several repeated Zn stripping/plating behaviors (Figs. S7–S8), corresponding to the beneficial inhibition of the HER on the electrode surface. These findings signify the substantially enhanced desolvation capability with the TiN@RGO catalytic layer, the improved anti-corrosion effect for the Zn electrode towards the

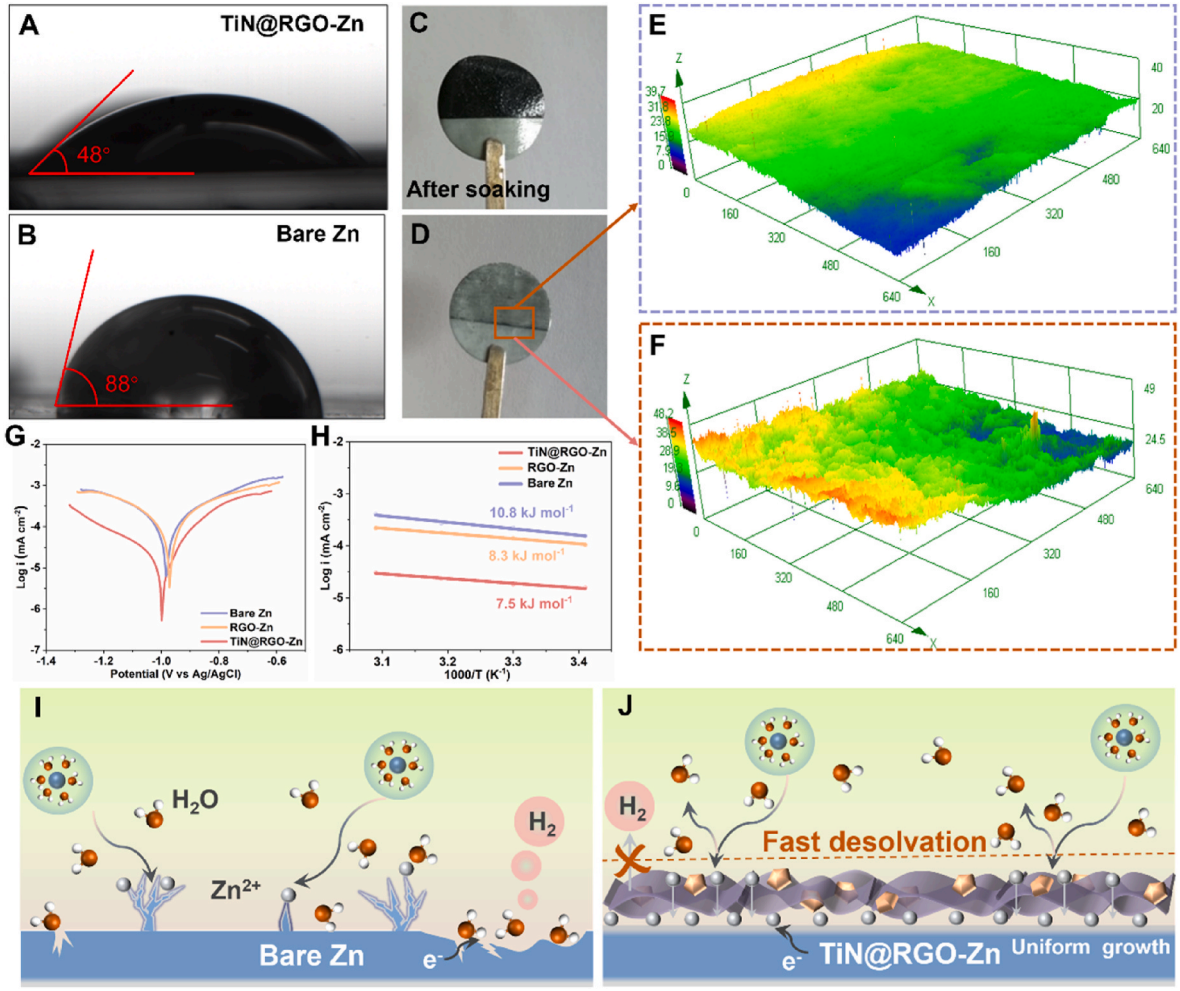

Fig. 2. (A) Comparing the contact angles of electrolyte on the surface of (A) TiN@RGO-Zn and (B) Bare Zn electrods; (C) Optical images of (C) TiN@RGO-Zn and exposed bare Zn after electrolyte immersion for three weeks, and (D) after removing the upper modified layer; Confocal microscopic 3D morphology of the immersed Zn (E) with (F) without upper TiN@RGO layer; (G) Tafel plots of TiN@RGO-Zn, RGO-Zn and Bare Zn tested on a three-electrode system; (H) Comparison of desolvation activation energy (*Ea*) calculated by Arrhenius equation on the TiN@RGO-Zn, RGO-Zn and Bare Zn interfaces; Schematic illustrations of (I) HER and dendrite growth on bare Zn electrode and (J) synergistic desolvation mechanism of "adsorption-sieving-catalysis" effect upon the TiN@RGO nano catalysts against side reactions and dendrite growth.

electrolyte and the effectively suppression of hydrogen evolution reaction. Like the literatures reported before [15,21,48], the catalytic sites in TiN are verified as effective means in reducing energy barriers to improve the $[Zn(H_2O)_6]^{2+}$ desolvation efficiency. In detail, the dissociation of hydrate $[Zn(H_2O)_x]^{2+}$ is significantly accelerated to avoid the formation of active water for generating HER due to the enhanced desolvation-diffusion kinetics upon the synergistic TiN@RGO artificial layer (Fig. 2I and J). Moreover, the abundant zincophilic and catalytic sites (TiN) with transport channels (RGO) are beneficial to synergistically decrease the energy barriers to provide superfast Zn^{2+} desolvation and diffusion, averaging the Zn^{2+} flux for smooth deposition against dendrite growth (Fig. 2J).

3.3. Dendrite-free performance of the catalytic TiN@RGO-Zn anodes

To assess the reversibility and sustainability of the TiN@RGO-Zn electrode, the Coulombic efficiency (CE) value was assessed on a TiN@RGO-Zn||Cu asymmetric cell. At a current density of 1 mA cm^{-2} with a cut-off potential of 1.0 V, the CE of TiN@RGO-Zn electrode reached as high as 99.72 % after 100 cycles in comparison to a short circuit after 20 cycles of the bare Zn electrode (Fig. 3A). Besides, the stable voltage polarization of the TiN@RGO-Zn electrode (60 mV) within 100 cycles showcases the TiN@RGO efficacy in suppressing side reactions due to the decreased active water moleculesafter dissociating by TiN@RGO catalytic layer (Fig. S9). Symmetric cells were then fabricated to assess the striping/plating stability of the TiN@RGO-Zn electrode. Initially, the TiN@RGO-Zn electrode with TiN loading of 20 wt% (named as 20-TiN@RGO-Zn) in Fig. S10 delivers the best cycling stability with quite smaller overpotential among others (with 5~15 wt% and 25 wt% loading). Thereafter, the optimal TiN@RGO-Zn electrode with 20 wt% TiN was selected and characterized throughout this work unless otherwise specified. With 20 wt% TiN loading, the Zn electrode

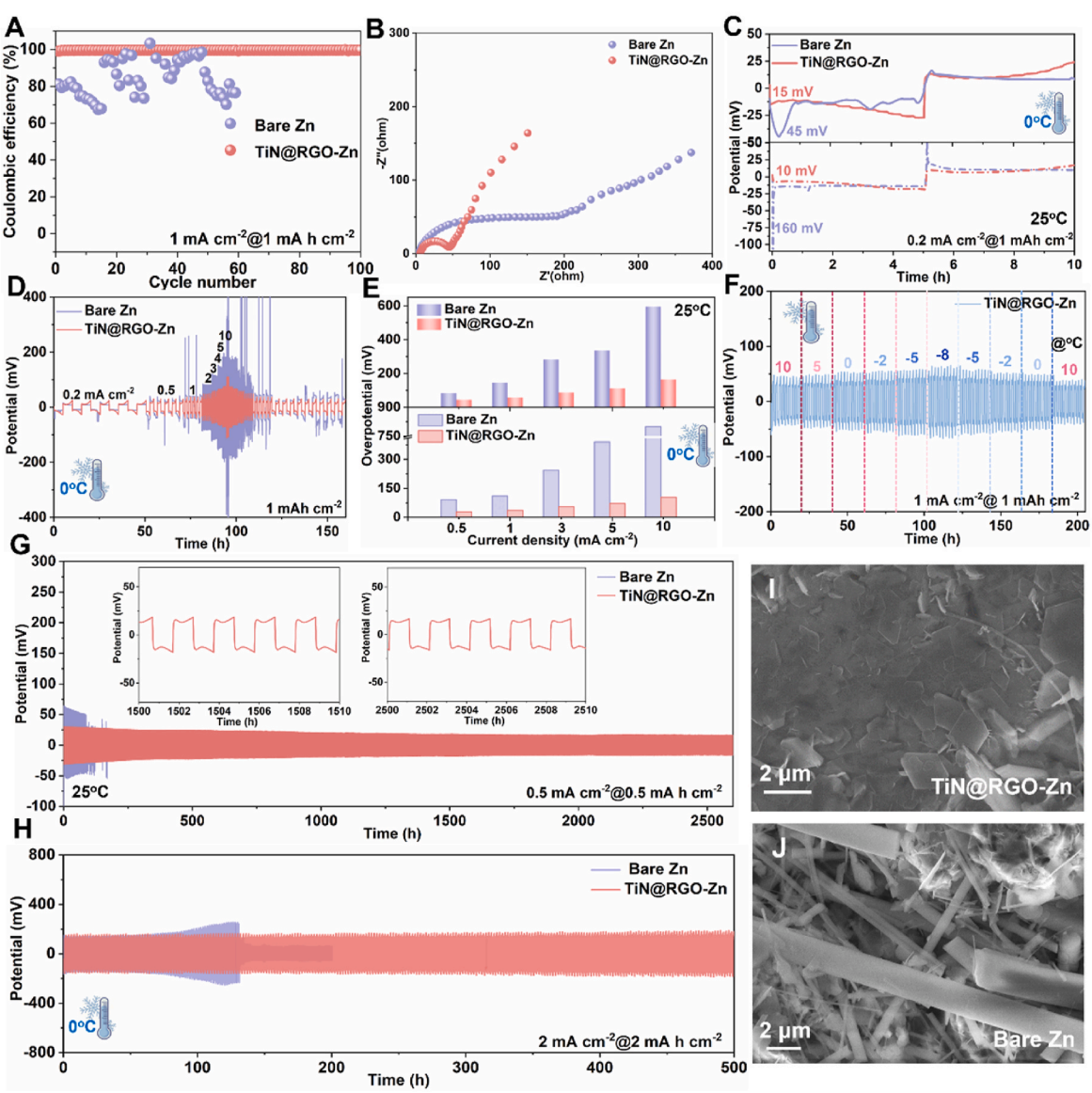

Fig. 3. (A) Coulombic efficiency (CE) measurements of the TiN@RGO-Zn||Cu and Zn||Cu asymmetric cells at 1 mA cm^{-2} with 1 mA h cm^{-2} at a cut-off potential of 1.0 V; (B) Comparison of EIS spectra of symmetrical cells based on different electrodes; (C) Initial nucleation potential of the TiN@RGO-Zn and bare Zn electrodes; (D) Rate performance of the TiN@RGO-Zn and bare Zn electrodes at a current range of 0.2–10 mA cm^{-2} under 0 °C; (E) Overpotential comparison on the TiN@RGO-Zn and bare Zn electrodes at a current range of 0.2–10 mA cm^{-2}; (F) Plating/striping performance of the two electrodes under 1 mA cm^{-2} with 1 mA h cm^{-2} at a shifting temperature from 0 to −8 °C; Cycling performances of the electrodes (G) under 0.5 mA cm^{-2} with 0.5 mA h cm^{-2} at room temperature and (H) under 2 A cm^{-2} with 2 mA h cm^{-2} at 0 °C; SEM images of Zn deposited on the surface of (I) TiN@RGO-Zn and (J) bare Zn.

coating 30 μm of TiN@RGO layer in Fig. S11 offers stable cycling with lower overpotential of 109 mV than those of 10 μm (124 mV) and 60 μm (176 mV). And the super P in the coating within the content of 10∼20 wt % reflect negligible impact on the coating integrity and electrochemical performance (Fig. S12). Then, the electrochemical reaction kinetics were evaluated by electrochemical impedance spectroscopy (Fig. 3B and Fig. S13). The TiN@RGO-Zn electrode exhibited significantly reduced charge transfer resistance (*Rct*) relative to RGO-Zn and bare Zn (40 vs 90 vs 173 Ω), indicating enhanced Zn^{2+} conductivity and transport kinetics by TiN@RGO modulation. The Zn^{2+} desolvation and diffusion kinetics are also reflected in the nucleation barrier of symmetric cells. The both nucleation barriers in the TiN@RGO-Zn electrodes at room temperature and low temperature are remarkably decreased (Fig. 3C). For example, under harsh condition of 0 °C, the TiN@RGO-Zn electrode still obtains the lower initial nucleation barrier (15 vs. 45 mV). Varying the current density, the TiN@RGO-Zn symmetric cell displays high current tolerance even to 10 mA cm^{-2} due to the stable increase of overpotentials with the increase of current density (Fig. S14). Lowering operation temperature to 0 °C, the TiN@RGO-Zn electrode also demonstrates stable plating/stripping process, due to the consistently lower and stable overpotentials compared to those of the bare Zn electrode with shifting current density from 0.2–10 mA cm^{-2} (Fig. 3D and E and S15). Even at a high current density of 10 mA cm^{-2}, the TiN@RGO-Zn electrode still delivers quite lower overpotential (223 mV vs 395 vs 800 mV), confirming its high-rate application prospects under low temperature (Figs. 3E and S15). More impressively, the TiN@RGO-Zn electrode delivers ultra strong temperature robustness due to the steady growing overpotential to no more than 130 mV even shifting temperature to ultra-low −8 °C without any dendrite growth (Fig. 3F). No matter at room temperature or low temperature, the TiN@RGO-Zn electrodes present enduring plating/striping performance. At room temperature, low overpotential of 50 mV with negligible voltage fluctuations after 2600 h under 0.5 mA cm^{-2} and 0.5 mA h cm^{-2} is exhibited, whereas the bare Zn only works normally for less than 200 h (Fig. 3G). Increasing the current density or deposition depth (1 mA cm^{-2}@1 mA h cm^{-2} or 3 mA cm^{-2}@2 mA h cm^{-2}), the TiN@RGO-Zn electrode can stabilize for 600 or 500 h with low overpotentials (81 mV or 202 mV) without any short-circuit, respectively (Fig. S16). The XRD pattern for the cycled TiN@RGO-Zn mainly presents the characteristic peaks of Zn located at 36.3°, 39.0° and 43.2°, attributing to the (002), (100) and (101) planes of standard metallic Zn (JCPDS 04–0831) phase instead of any other corrosion substance (Fig. S17). Decreasing to low temperature of 0 °C, the TiN@RGO-Zn electrode still demonstrates a stable and small overpotential of 160 mV during more than 1250 h cycling with the current density of 0.5 mA cm^{-2} and areal specific capacity of 0.5 mA h cm^{-2} (Fig. S18). As a contrast, the RGO-Zn and bare Zn electrodes displayed erratic voltage fluctuations and rapid cell failures after 900 and 590 h due to short circuit or excessive polarization coming from dendrite growth and "dead" Zn during deposition. Even increasing the current densities/depth of discharge (DOD) to 2 mA cm^{-2}/2 mA h cm^{-2}, the symmetrical cell based on TiN@RGO-Zn electrode could cycle stably for 500 h despite the rapid failure of the bare Zn electrode with sharply raised overpotential within no more than 150 h (Fig. 3H). Overall, the TiN@RGO-Zn electrodes showcase a steady voltage curve over a long cycling life with a temperature robustness, indicating stable and smooth Zn deposition at the electrode interface owning to the fast Zn^{2+} desolvation and diffusion catalyzed by TiN@RGO layer. As a confirmation, SEM image of the cycled TiN@RGO-Zn electrode maintains a dense and compact surface devoid of zinc dendrite formation (Fig. 3I), owing to that the generated metal atoms are capable of penetrating through the catalytic layer and reaching the bottom Zn metal for lateral deposition. In contrast, the rugged surface of the RGO-Zn surface as well as a plenty of Zn dendrites on the bare Zn surface are observed (Figs. 3J and S19). In spite of the weakened sieving process of RGO under low temperature, the TiN with intrinsic high electron/ion conductivity enables robust catalytic property to break the Zn^{2+}-H_2O bonds and take off H_2O molecules and other unwanted anion for liberating affluent free Zn^{2+} for uniform electrodeposition.

3.4. Electrochemical performance of the TiN@RGO-Zn||MnO_2 full cells

Then, the practical application potential of the TiN@RGO catalysis layer in a TiN@RGO-Zn||MnO_2 full cell was evaluated. Initially, the EIS curves (Figs. 4A and S20) disclose a significantly lower *Rct* of 15 Ω for the TiN@RGO-Zn||MnO_2 full cell compared to 105 and 180 Ω for the RGO-Zn||MnO_2 and bare Zn|| MnO_2 full cells, signifying a faster charge and ion transfer kinetics catalyzed by TiN@RGO. The CV curves in Figs. 4B and S21 show two pairs of redox peaks which corresponds to the two-step reverse oxidation/reduction between MnO_2 and MnOOH. The lower distance between the redox reaction peaks and higher intensity of the current peaks in the TiN@RGO-Zn||MnO_2 full cell, indicating a smaller polarization (0.33 vs 0.4 vs 0.45 V) and faster reaction kinetics than the RGO-Zn||MnO_2 and bare Zn||MnO_2 full cells, owing to faster interfacial Zn^{2+} desolvation and diffusion kinetics catalyzed by the TiN@RGO layer during the plating/stripping process. In the following scanning, the TiN@RGO-Zn||MnO_2 cell still shows good overlap within 4 cycles (Fig. S22), which indicates the effectively improvement to the reversibility of the redox reaction facilitated by the enhanced interfacial Zn^{2+} desolvation and diffusion. Shifting scanning rate from 0.1 to 1 mV s^{-1} (Figs. 4C and S23), the TiN@RGO modulated cell exhibits higher Zn ion diffusion kinetics with larger linear slop obtained on the oxidation peaks (3.0 vs 2.7), benefiting the cell with remarkably improved rate performance. As depicted in Fig. 4D, the TiN@RGO-Zn||MnO_2 cell maintains 99 % of its initial capacity after 24 h resting compared to 89 % of untreated Zn||MnO_2 cell. Thereafter, the TiN@RGO-Zn||MnO_2 cell delivers the discharge capacities of 380, 305, 262, 215, 169, and 140 mA h g^{-1} at 0.1, 0.3, 0.5, 1, 2 and 3 A g^{-1}, respectively, which is much higher than that of the bare Zn||MnO_2 cell under the same conditions (Fig. S24). Stabilizing a high current density of 1 A g^{-1}, the TiN@RGO-Zn||MnO_2 full cell displays a high initial capacity of 271 mA h g^{-1} and following a remarkable capacity retention of nearly 100 % after 300 cycles, while the bare Zn||MnO_2 cell has an inferior initial capacity of 149 mA h g^{-1} with poor capacity retention of merely 34 % (Fig. 4E and S25-S26). Decreasing to harsh condition of 0 °C, the TiN@RGO-Zn|| MnO_2 cell still manifests a superior rate performance than the bare Zn|| MnO_2 cell, delivering a specific capacity of 203 mA h g^{-1}, 127 mA h g^{-1} and 98 mA h g^{-1} at 0.5, 1.5, and even 2 A g^{-1} (Fig. 4F). Upon reverting to a current density of 0.5 A g^{-1}, the discharge capacity restored to 223 mA h g^{-1}, highlighting the high reversibility and fast interfacial Zn^{2+} desolvation and diffusion for TiN@RGO-Zn anode. The long-term cycle stability of the TiN@RGO-Zn||MnO_2 cell under low temperature is also impressive, rendering an initial capacity of 175 mA h g^{-1} at 1.0 A g^{-1} with a high capacity retention of nearly 72 % with a low capacity decay rate of merely 0.028 % per cycle after 1000 cycles (Fig. 4G). The above results well corroborate that constructing TiN@RGO catalytic layer can effectively enhance the interfacial Zn^{2+} desolvation and diffusion to promote the stability and rate capability of low temperature Zn ion batteries.

4. Conclusion

In summary, the strategy of "adsorption-sieving-catalysis" is successfully achieved in protecting Zn surface, of which the titanium nitride anchored on self-assembly porous reduced graphene oxide (TiN@RGO) as electrocatalyst modulator provides reversible capability in plating and stripping of Zn against dendrite growth. The TiN@RGO catalytic layer can guide the uniform growth of zinc and effectively block the formation of zinc dendrites and intricate side reactions of HER and electrode corrosion simultaneously. Consequently, the TiN@RGO-Zn electrode discloses a significantly accelerated Zn^{2+} deposition kinetics and lower nucleation potential (15 mV vs 45 mV) with a dendrite-free surface, extending the lifespan above 2600 h at 0.5 mA cm^{-2} and

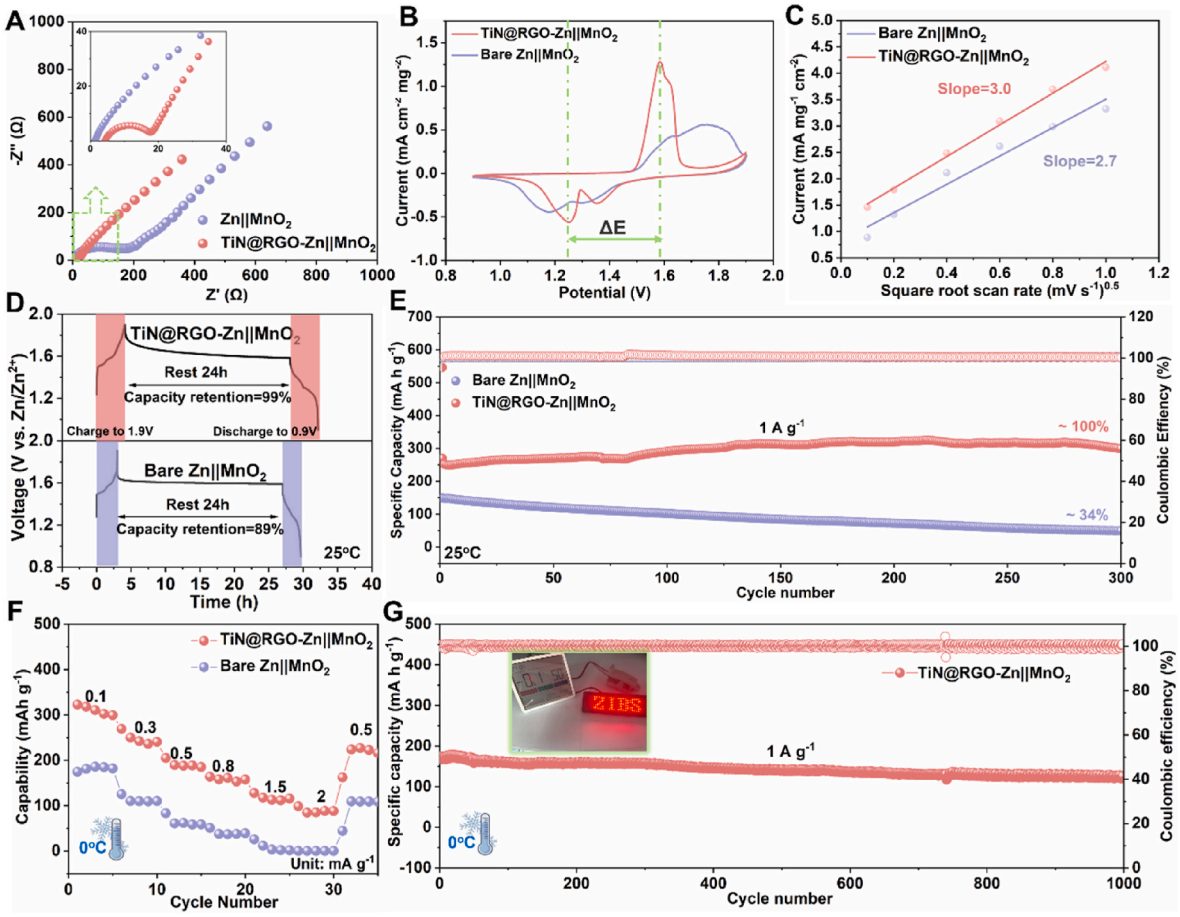

Fig. 4. Comparison of (A) EIS spectra and (B) CV curves at 0.1 mV s^{-1} for full cells based on TiN@RGO-Zn and bare Zn anodes; (C) Plot of the peak current density recorded at the anodic current peak versus the square root of the scan rates; (D) Self-discharge behavior of full cells under resting for 24 h; (E) Comparison of cycle performance of full cells based on TiN@RGO-Zn and bare Zn anodes at room temperature; (F) Comparison of rate performance and (G) long-term cycle stability of the TiN@RGO-Zn||MnO_2 full cell under low temperature of 0 °C.

maintaining reversible stability of 500 h at 2 mA cm^{-2} under low temperature of 0 °C. The coupled TiN@RGO-Zn full cell presents a high capacity retention of nearly 72 % after 1000 cycles at 1.0 A g^{-1} at 0 °C, underlining the potential application of AZMBs.

CRediT authorship contribution statement

Jing Zhang: Writing – original draft, Project administration, Investigation, Formal analysis. **Chenxiao Han:** Methodology, Formal analysis, Data curation. **Lu Pan:** Methodology, Formal analysis, Data curation. **Mannan Yang:** Methodology, Investigation, Formal analysis. **Caiyin You:** Writing – review & editing, Methodology. **Yongzheng Zhang:** Validation, Formal analysis, Data curation. **Lujie Jia:** Validation, Formal analysis, Data curation. **Huihua Li:** Software, Methodology, Investigation. **Ke Xu:** Software, Methodology, Investigation. **Jian Su:** Methodology, Investigation, Formal analysis. **Hongzhen Lin:** Writing – review & editing, Validation, Supervision, Resources, Project administration, Methodology, Investigation, Funding acquisition. **Jian Wang:** Writing – review & editing, Validation, Supervision, Resources, Project administration, Methodology, Investigation, Funding acquisition.

Declaration of competing interest

The authors declare that they have no known competing financial interests or personal relationships that could have appeared to influence the work reported in this paper.

Acknowledgements

The authors acknowledge financial support from the National Natural Science Foundation of China (No. 22309144, 52371198, 21972164, 22279161), the Natural Science Foundation of Jiangsu Province (BK. 20210130), the Key R&D Program of Jiangsu Province (BG2024020), Suzhou Science and Technology Plan projects (SYC2022057), Opening funding from Key Laboratory of Engineering Dielectrics and Its Application (Harbin University of Science and Technology) (No. KFM202507, Ministry of Education), China Postdoctoral Science Foundation (No. 2023M732561, 2023M731084), Shanghai Sailing Program of China (23YF1408900). J. Wang thanks the fellowship support provided by the Alexander von Humboldt Foundation. The authors are also grateful for the technical support from Advanced Material Analysis and Test Center of Xi'an University of Technology, and Nano-X, Suzhou Institute of Nano-tech and Nano-bionics, Chinese Academy of Sciences.

Appendix A. Supplementary data

Supplementary data to this article can be found online at https://doi.org/10.1016/j.jpowsour.2025.236810.

Data availability

Data will be made available on request.

References

[1] H. Yan, S. Li, Y. Nan, S. Yang, B. Li, Ultrafast zinc-ion-conductor interface toward high-rate and stable zinc metal batteries, Adv. Energy Mater. 11 (18) (2021) 2100186.

[2] C. Ma, X. Wang, W. Lu, C. Wang, H. Yue, G. Sun, D. Zhang, F. Du, Achieving stable Zn metal anode via a simple nico layered double hydroxides artificial coating for high performance aqueous Zn-ion batteries, Chem. Eng. J. 429 (2022) 132576.

[3] K. Zhang, C. Li, J. Liu, S. Zhang, M. Wang, L. Wang, Defect-rich functional HfO_{2-x} for highly reversible Zn metal anode, Small 20 (14) (2023) 2306406.

[4] Z. Chen, Y. Wang, Q. Wu, C. Wang, Q. He, T. Hu, X. Han, J. Chen, Y. Zhang, J. Chen, L. Yang, X. Wang, Y. Ma, J. Zhao, Grain boundary filling empowers (002)-textured Zn metal anodes with superior stability, Adv. Mater. 36 (46) (2024) 2411004.

[5] Y. Zhang, Z. Cao, S. Liu, Z. Du, Y. Cui, J. Gu, Y. Shi, B. Li, S. Yang, Charge-enriched strategy based on MXene-based polypyrrole layers toward dendrite-free zinc metal anodes, Adv. Energy Mater. 12 (13) (2022) 2103979.

[6] T. Wang, Q. Xi, Y. Li, H. Fu, Y. Hua, E.G. Shankar, A.K. Kakarla, J.S. Yu, Regulating dendrite-free zinc deposition by red phosphorous-derived artificial protective layer for zinc metal batteries, Adv. Sci. 9 (18) (2022) 2200155.

[7] J. Xu, H. Li, Y. Jin, D. Zhou, B. Sun, M. Armand, G. Wang, Understanding the electrical mechanisms in aqueous zinc metal batteries: from electrostatic interactions to electric field regulation, Adv. Mater. 36 (3) (2023) 2309726.

[8] Z. Zhao, H. Zhang, X. Shi, Y. Zhang, C. Tang, H. Zhao, J. Liu, G. Wang, L. Li, Zincophilic metal-organic-framework interface mitigating dendrite growth for highly reversible zinc metal batteries, Small 20 (6) (2023) 2304723.

[9] K. Wang, F. Liu, Q. Li, J. Zhu, T. Qiu, X.-X. Liu, X. Sun, An electrolyte additive for interface regulations of both anode and cathode for aqueous zinc-vanadium oxide batteries, Chem. Eng. J. 452 (2023) 139577.

[10] J. Cao, Y. Sun, D. Zhang, D. Luo, L. Zhang, R. Chanajaree, J. Qin, X. Yang, J. Lu, Interfacial double-coordination effect guiding uniform electrodeposition for reversible zinc metal anode, Adv. Energy Mater. 14 (2) (2023) 2302770.

[11] C.-C. Kao, C. Ye, J. Hao, J. Shan, H. Li, S.-Z. Qiao, Suppressing hydrogen evolution via anticatalytic interfaces toward highly efficient aqueous Zn-ion batteries, ACS Nano 17 (4) (2023) 3948–3957.

[12] J. Cao, X. Wang, S. Qian, D. Zhang, D. Luo, L. Zhang, J. Qin, X. Zhang, X. Yang, J. Lu, De-passivation and surface crystal plane reconstruction via chemical polishing for highly reversible zinc anodes, Adv. Mater. 36 (46) (2024) 2410947.

[13] L. Wang, F. Wang, Z. Ding, Y. Liu, Z. Zhang, C. Yang, K.P. Loh, Q.-H. Yang, Bilayer separator enabling dendrite-free zinc anode with ultralong lifespan >5000 h, Green Energy Environ. 9 (4) (2024) 771–776.

[14] L. Jia, H. Hu, X. Cheng, H. Dong, H. Li, Y. Zhang, H. Zhang, X. Zhao, C. Li, J. Zhang, H. Lin, J. Wang, Toward low-temperature zinc-ion batteries: strategy, progress, and prospect in vanadium-based cathodes, Adv. Energy Mater. 14 (8) (2023) 2304010.

[15] X. Cheng, Y. Zuo, Y. Zhang, X. Zhao, L. Jia, J. Zhang, X. Li, Z. Wu, J. Wang, H. Lin, Superfast zincophilic ion conductor enables rapid interfacial desolvation kinetics for low-temperature zinc metal batteries, Adv. Sci. 11 (28) (2024) 2401629.

[16] Z. Hou, Z. Lu, Q. Chen, B. Zhang, Realizing wide-temperature Zn metal anodes through concurrent interface stability regulation and solvation structure modulation, Energy Storage Mater. 42 (2021) 517–525.

[17] R. Zhang, Y. Feng, Y. Ni, B. Zhong, M. Peng, T. Sun, S. Chen, H. Wang, Z. Tao, K. Zhang, Bifunctional interphase with target-distributed desolvation sites and directionally depositional ion flux for sustainable zinc anode, Angew. Chem. Int. Ed. 62 (25) (2023) 2304503.

[18] H. Li, S. Li, R. Hou, Y. Rao, S. Guo, Z. Chang, H. Zhou, Recent advances in zinc-ion dehydration strategies for optimized Zn-metal batteries, Chem. Soc. Rev. 53 (15) (2024) 7742–7783.

[19] M. Zhang, W. Xu, X. Han, H. Fan, T. Chen, Y. Yang, Y. Gao, C. Zheng, Y. Yang, T. Xiong, Y.W. Zhang, W.S.V. Lee, W. Wang, H. Pan, Z.G. Yu, J. Xue, Unveiling the mechanism of the dendrite nucleation and growth in aqueous zinc ion batteries, Adv. Energy Mater. 14 (9) (2023) 2303737.

[20] L. Yao, J. Liu, F. Zhang, B. Wen, X. Chi, Y. Liu, Reconstruction of zinc-metal battery solvation structures operating from $-50 \sim +100\ ^{o}C$, Nat. Commun. 15 (1) (2024) 6249.

[21] J. Wang, H. Hu, L. Jia, J. Zhang, Q. Zhuang, L. Li, Y. Zhang, D. Wang, Q. Guan, H. Hu, M. Liu, L. Zhan, H. Adenusi, S. Passerini, H. Lin, Fast interfacial electrocatalytic desolvation enabling low-temperature and long-cycle-life aqueous Zn batteries, InfoMat 6 (7) (2024) e12558.

[22] Y. Qiu, X. Zheng, R. Zhang, Q. Lin, M. Li, J. Luo, S. Yang, Z. Liu, Q. Wang, Y. Yu, C. Yang, Boosting zinc-ion batteries with innovative ternary electrolyte for enhanced interfacial electrochemistry and temperature-resilient performance, Adv. Funct. Mater. 34 (4) (2023) 2310825.

[23] J. Chen, S. Li, F. Li, W. Sun, Z. Nie, B. Xiao, Y. Cheng, X. Xu, Integrated interfacial modulation strategy: trace sodium hydroxyethyl sulfonate additive for extended-life Zn anode based on anion adsorption and electrostatic shield, ACS Appl. Mater. Interfaces 16 (32) (2024) 42153–42163.

[24] N. Zhang, S. Huang, Z. Yuan, J. Zhu, Z. Zhao, Z. Niu, Direct self-assembly of MXene on Zn anodes for dendrite-free aqueous zinc-ion batteries, Angew. Chem. Int. Ed. 60 (6) (2020) 2861–2865.

[25] S. So, Y.N. Ahn, J. Ko, I.T. Kim, J. Hur, Uniform and oriented zinc deposition induced by artificial Nb_2O_5 layer for highly reversible Zn anode in aqueous zinc ion batteries, Energy Storage Mater. 52 (2022) 40–51.

[26] X. Zheng, T. Ahmad, W. Chen, Challenges and strategies on Zn electrodeposition for stable Zn-ion batteries, Energy Storage Mater. 39 (2021) 365–394.

[27] C. Li, X. Cheng, Y. Zhang, J. Zhu, H. Zhou, Y. Yang, J. Xu, J. Wang, Y. Wang, H. Yu, C. Shen, L. Zhan, L. Ling, Towards low-temperature dendrite-free zinc anode by constructing functional mxene buffer layer with duplex zincophilic sites, J. Colloid Interface Sci. 671 (2024) 505–515.

[28] M. Han, T.C. Li, X. Chen, H.Y. Yang, Electrolyte modulation strategies for low-temperature Zn batteries, Small 20 (3) (2023) 2304901.

[29] Y. Yang, C. Liu, Z. Lv, H. Yang, X. Cheng, S. Zhang, M. Ye, Y. Zhang, L. Chen, J. Zhao, C.C. Li, Redistributing Zn-ion flux by interlayer ion channels in Mg-Al layered double hydroxide-based artificial solid electrolyte interface for ultra-stable and dendrite-free Zn metal anodes, Energy Storage Mater. 41 (2021) 230–239.

[30] Y. Chu, S. Zhang, S. Wu, Z. Hu, G. Cui, J. Luo, In situ built interphase with high interface energy and fast kinetics for high performance Zn metal anodes, Energy Environ. Sci. 14 (6) (2021) 3609–3620.

[31] Q. Zong, B. Lv, C. Liu, Y. Yu, Q. Kang, D. Li, Z. Zhu, D. Tao, J. Zhang, J. Wang, Q. Zhang, G. Cao, Dendrite-free and highly stable Zn metal anode with $BaTiO_3$/P(VDF-TrFE) coating, ACS Energy Lett. 8 (7) (2023) 2886–2896.

[32] L. Li, H. Tu, J. Wang, M. Wang, W. Li, X. Li, F. Ye, Q. Guan, F. Zhu, Y. Zhang, Y. Hu, C. Yan, H. Lin, M. Liu, Electrocatalytic MOF-carbon bridged network accelerates Li^+-Solvents desolvation for high Li^+ diffusion toward rapid sulfur redox kinetics, Adv. Funct. Mater. 33 (13) (2023) 2212499.

[33] K. Yan, Y. Fan, F. Hu, G. Li, X. Yang, X. Wang, X. Li, C. Peng, W. Wang, H. Fan, L. Ma, A "polymer-in-salt" solid electrolyte enabled by fast phase transition route for stable Zn batteries, Adv. Funct. Mater. 34 (2) (2023) 2307740.

[34] X. He, Y. Qian, Y. Wu, Z. Yan, X. Lin, X.Y. Kong, Y. Zhao, L. Jiang, L. Wen, Metal-phosphonate-organic network as ion enrichment layer for sustainable zinc metal electrode with high rate capability, Angew. Chem. Int. Ed. 63 (50) (2024) 2411563.

[35] C. Li, X. Jiang, H. Qi, D. Chen, T. You, S. Huang, H. Yu, Y. Huang, M. Rao, G. Li, B. Xu, Y. Chen, L. Chen, Interfacial dual-modulation through deoxygenation effect and tuning hydrogen-bonding environment toward highly reversible Zn metal anodes, Energy Storage Mater. 75 (2025) 104012.

[36] X. Li, Z. Chen, P. Ruan, X. Hu, B. Lu, X. Yuan, S. Tian, J. Zhou, Inducing preferential growth of the Zn (002) plane by using a multifunctional chelator for achieving highly reversible Zn anodes, Nanoscale 16 (6) (2024) 2923–2930.

[37] W. Wang, S. Chen, X. Liao, R. Huang, F. Wang, J. Chen, Y. Wang, F. Wang, H. Wang, Regulating interfacial reaction through electrolyte chemistry enables gradient interphase for low-temperature zinc metal batteries, Nat. Commun. 14 (1) (2023) 5443.

[38] W. Zhang, Q. Dong, J. Wang, X. Han, W. Hu, Failure mechanism, electrolyte design, and electrolyte/electrode interface regulation for low-temperature zinc-based batteries, Small Methods 7 (10) (2023) 2300324.

[39] Y. Wang, Y. Fan, D. Liao, Y. Wu, Y. Yu, C. Hu, Highly Zn^{2+}-conductive and robust modified montmorillonite protective layer of electrodes toward high-performance rechargeable zinc-ion batteries, Energy Storage Mater. 51 (2022) 212–222.

[40] M. Fu, Q. Zhao, K. Long, Q. Li, G.c. Kuang, L. Zhou, W. Wei, X. Ji, L. Chen, Y. Chen, Global "interface-space" dual-modulation by functional supramolecules organic frameworks on aqueous zinc-ion batteries, Adv. Funct. Mater. 34 (10) (2023) 2311680.

[41] T. Wang, P. Wang, L. Pan, Z. He, L. Dai, L. Wang, S. Liu, S.C. Jun, B. Lu, S. Liang, J. Zhou, Stabling zinc metal anode with polydopamine regulation through dual effects of fast desolvation and ion confinement, Adv. Energy Mater. 13 (5) (2022) 2203523.

[42] J. Yu, C. Chen, F. Shi, R. Li, F. Chen, J. Tang, K.C. Chan, Z.-L. Xu, A multifunctional MXene-porous polydopamine interface for stable and dendrite-free zinc metal batteries, Energy Storage Mater. 63 (2023) 102966.

[43] Z. Zheng, X. Zhong, Q. Zhang, M. Zhang, L. Dai, X. Xiao, J. Xu, M. Jiao, B. Wang, H. Li, Y. Jia, R. Mao, G. Zhou, An extended substrate screening strategy enabling a low lattice mismatch for highly reversible zinc anodes, Nat. Commun. 15 (1) (2024) 753.

[44] W. Xin, J. Xiao, J. Li, L. Zhang, H. Peng, Z. Yan, Z. Zhu, Metal-organic frameworks with carboxyl functionalized channels as multifunctional ion-conductive interphase for highly reversible Zn anode, Energy Storage Mater. 56 (2023) 76–86.

[45] W. Xu, J. Li, X. Liao, L. Zhang, X. Zhang, C. Liu, K. Amine, K. Zhao, J. Lu, Fluoride-rich, organic–inorganic gradient interphase enabled by sacrificial solvation shells for reversible zinc metal batteries, J. Am. Chem. Soc. 145 (41) (2023) 22456–22465.

[46] H. Sun, Y. Huyan, N. Li, D. Lei, H. Liu, W. Hua, C. Wei, F. Kang, J.-G. Wang, A seamless metal-organic framework interphase with boosted Zn^{2+} flux and deposition kinetics for long-living rechargeable Zn batteries, Nano Lett. 23 (5) (2023) 1726–1734.

[47] F. Zhu, J. Wang, Y. Zhang, H. Tu, X. Xia, J. Zhang, H. He, H. Lin, M. Liu, Low-temperature lithium metal batteries achieved by synergistically enhanced screening Li^+ desolvation kinetics, Adv. Mater. (2024) 2411601.

[48] J. Wang, J. Zhang, J. Wu, M. Huang, L. Jia, L. Li, Y. Zhang, H. Hu, F. Liu, Q. Guan, M. Liu, H. Adenusi, H. Lin, S. Passerini, Interfacial "single-atom-in-defects" catalysts accelerating Li^+ desolvation kinetics for long-lifespan lithium-metal batteries, Adv. Mater. 35 (39) (2023) 2302828.

[49] J. Wang, J. Zhang, Y. Zhang, H. Li, P. Chen, C. You, M. Liu, H. Lin, S. Passerini, Atom-level tandem catalysis in lithium metal batteries, Adv. Mater. 36 (26) (2024) 2402792.

[50] C. Yan, H.-R. Li, X. Chen, X.-Q. Zhang, X.-B. Cheng, R. Xu, J.-Q. Huang, Q. Zhang, Regulating the inner Helmholtz plane for stable solid electrolyte interphase on lithium metal anodes, J. Am. Chem. Soc. 141 (23) (2019) 9422–9429.

[51] Q. Zhao, W. Liu, X. Ni, H. Yu, C. Zhang, B. Wang, L. Jiang, H. He, Y. Chen, L. Chen, Steering interfacial renovation with highly electronegative Cl modulated trinity effect for exceptional durable zinc anode, Adv. Funct. Mater. 34 (41) (2024) 2404219.

[52] X. Yang, H. Fan, F. Hu, S. Chen, K. Yan, L. Ma, Aqueous zinc batteries with ultra-fast redox kinetics and high iodine utilization enabled by iron single atom catalysts, Nano-Micro Lett. 15 (1) (2023) 126.
[53] Z. Cui, C. Zu, W. Zhou, A. Manthiram, J.B. Goodenough, Mesoporous titanium nitride-enabled highly stable lithium-sulfur batteries, Adv. Mater. 28 (32) (2016) 6926–6931.
[54] Q. Jiao, T. Zhou, N. Zhang, S. Liu, Q. Huang, W. Bi, W. Chu, X. Wu, Y. Zhu, Y. Feng, C. Wu, High-surface-area titanium nitride nanosheets as zinc anode coating for dendrite-free rechargeable aqueous batteries, Sci. China Mater. 65 (7) (2022) 1771–1778.
[55] J. Zheng, Z. Cao, F. Ming, H. Liang, Z. Qi, W. Liu, C. Xia, C. Chen, L. Cavallo, Z. Wang, H.N. Alshareef, Preferred orientation of TiN coatings enables stable zinc anodes, ACS Energy Lett. 7 (1) (2021) 197–203.
[56] J. Zhang, C. You, W. Zhang, J. Wang, S. Guo, R. Yang, Y. Xu, Conductive bridging effect of TiN nanoparticles on the electrochemical performance of TiN@CNT-S composite cathode, Electrochim. Acta 250 (2017) 159–166.